JGR Space Physics

RESEARCH ARTICLE
10.1029/2020JA028166

Key Points:
- This study presents a new method of estimating polar cap electron density based on passive radio measurements
- Auroral medium-frequency burst typically originates around 200 km: median source heights range from 139 to 296 km with a mean of 208 km
- Burst sources appear to be on the topside of the density peak, but the profile peaks in the *E* region rather than the *F* region

Correspondence to:
A. C. Burnett,
acb18@stanford.edu

Citation:
Burnett, A. C., & LaBelle, J. (2020). Estimating polar cap density and medium-frequency burst source heights using $2f_{ce}$ roar radio emissions. *Journal of Geophysical Research: Space Physics*, *125*, e2020JA028166. https://doi.org/10.1029/2020JA028166

Received 23 MAY 2020
Accepted 25 AUG 2020
Accepted article online 28 SEP 2020

Estimating Polar Cap Density and Medium-Frequency Burst Source Heights Using $2f_{ce}$ Roar Radio Emissions

Adam C. Burnett[1,2] **and James LaBelle**[1]

[1]Department of Physics and Astronomy, Dartmouth College, Hanover, NH, USA, [2]Department of Earth System Science, Stanford University, Stanford, CA, USA

Abstract Competing theories exist for the generation mechanism of auroral medium-frequency burst (MFB). In an effort to constrain MFB source heights, this study analyzes 33 events in which MFB and auroral $2f_{ce}$ roar co-occurred at Sondrestrom, Greenland. Using measurements from an array of receiving antennas, direction-of-arrival calculations indicate that in a given co-occurrence, the elevation angle of MFB typically is higher than that of roar. Ray tracing is used to determine source heights of the MFB signals. Density profiles are obtained from the International Reference Ionosphere (IRI) and shifted in magnitude until each event's roar signals originate at heights where the frequency-matching condition for $2f_{ce}$ roar generation is satisfied. This shifting method is validated using density measurements from the Sondrestrom incoherent scatter radar (ISR) facility for the two events with available ISR data. After shifting, ray tracing demonstrates that in 25 of the 33 events, burst originates at a height of about 200 km, lower than the typical altitude of peak electron density. However, ISR measurements show that the density profile is enhanced at low altitudes while MFB is observed, peaking in the *E* region rather than the *F* region. This finding implies that the MFB sources at 200 km are on the topside of the density peak, in a region of downward pointing density gradient, in qualitative agreement with the mechanism of MFB generation by Langmuir waves in the topside ionosphere. These results also suggest a new method of estimating density in the polar cap using roar signals to calibrate IRI profiles.

Plain Language Summary Auroral substorms, which produce the northern lights, also emit radio waves. This study focuses on two types of auroral radio emissions, called roar and burst. Various mechanisms have been proposed to explain burst, and they disagree about its altitude of origin. This study tests these theories by determining burst source heights. An antenna array in Sondrestrom, Greenland, is used to detect roar and burst signals. Their directions of origin are calculated based on the antenna configuration, and the rays are traced backward to their origin. This ray tracing relies on electron density estimates provided by the International Reference Ionosphere (IRI). To make the IRI data more accurate, density values are shifted so that roar rays are traced to their known source altitudes. This method of shifting the IRI profile using roar is a novel way of estimating electron density and is validated using measurements from the incoherent scatter radar system in Sondrestrom. Density measurements also show that as burst occurs, the density peaks at low altitude, below 200 km, whereas burst originates around 200 km in most of the events analyzed. This result provides observational support for theories predicting that burst generation occurs above the altitude of peak electron density.

1. Introduction

Earth's aurora emits several types of radio emissions ranging from relatively weak auroral roar, medium-frequency burst (MFB), and hiss to auroral kilometric radiation which comprises up to 1–2% of auroral energy. Some of these signals play important roles in space physics through wave-particle interactions, but even the relatively weak types, once they are understood, may provide effective techniques to remotely sense ionospheric plasma conditions and processes.

Auroral "roar", also known as cyclotron harmonic emissions, is one of the best-known auroral radio emissions, first observed from ground level by Kellogg and Monson (1979) but known previously from spacecraft observations (Benson & Wong, 1987; James et al., 1974). The most common emission occurs at $2f_{ce}$, around 3 MHz, during nighttime. Subsequent investigations discovered similar emission at $3f_{ce}$ during nighttime or twilight (Weatherwax et al., 1993), and $4f_{ce}$ (Sato et al., 2012) and $5f_{ce}$ (LaBelle, 2012) during daytime. The mechanism behind most of these emissions, proposed by Kaufmann (1980) and refined by Yoon et al. (1996), Yoon, Weatherwax, and Rosenberg (1998), and Yoon, Weatherwax, Rosenberg, LaBelle, et al. (1998), starts with instability, in the presence of a loss cone or horseshoe-type electron distribution function, of upper hybrid waves at the "double resonance" condition $f = f_{uh} = Nf_{ce}$, where $N = 2, 3, 4$, or 5. These waves subsequently convert to L-mode electromagnetic radiation through refraction to the "Ellis window" condition (Budden, 1985), which allows a linear mode conversion. This mechanism has been verified by ray tracing from above (James et al., 1974) and below (Hughes & LaBelle, 2001) the source region, as well as from a wide range of other evidence reviewed by LaBelle and Treumann (2002). The mechanism is also supported by in situ observations from a rocket flight that serendipitously penetrated a source region (Samara et al., 2004). This mechanism and the evidence supporting it establish that auroral roar originates at the double resonance condition, an altitude that can be predicted from the emission frequency and the altitude profile of the geomagnetic field. For the $2f_{ce}$ emission, the source height of roar typically lies around 275 km, depending on location (Hughes & LaBelle, 1998).

In contrast, MFB is probably the least known auroral emission. First identified in ground-level observations by Weatherwax et al. (1994), it also possibly has been remotely sensed from space (Broughton et al., 2015; Sato et al., 2010) and may have been incidentally detected in earlier ground-level experiments (e.g., Benson & Desch, 1991; Kellogg & Monson, 1979). MFB is broadband, typically spanning >1 MHz in the range 1.5–4.5 MHz. Like auroral roar, it is left-hand polarized (Shepherd et al., 1997). However, its generation mechanism has never been identified using in situ data, presumably because its duration is short and its source region may be confined both temporally and spatially to substorm onset. The strongest clue to a generation mechanism is its fine frequency structure on time scales of a few tens of milliseconds. This fine structure can take on a variety of forms but is sometimes dominated by descending tones (Bunch & LaBelle, 2009). This observation has led to speculation about a mechanism whereby Alfvénically accelerated electron beams with energy on the order of a few hundred electron volts excite Langmuir waves, over a range of altitudes, which subsequently convert to L-mode radiation, and the combination of electron and (primarily) wave dispersion produces the descending tones (LaBelle, 2011). Some experimental (Broughton et al., 2012) and modeling (Broughton et al., 2016) evidence supports this mechanism. Recently, a correlation has been observed between MFB and Langmuir "caviton" turbulence, concentrated at particular altitudes near 200–300 km in the auroral ionosphere (Akbari et al., 2013). If the cavitons radiate to produce MFB, the source might be concentrated rather than distributed in altitude. Alternatively, the relationship between MFB and cavitons may not be causal, but both may arise from the same conditions in substorm arcs.

Understanding of the MFB generation mechanism would benefit enormously if the emission source altitude or altitude distribution could be measured. On the other hand, the source altitude of auroral roar, which often coincides with MFB, is known precisely as described above. The original motivation of this research was to compare the directions of arrival of coincident or nearly coincident auroral roar and MFB, using high-frequency (HF) interferometry, in order to exploit the known source altitude of the former to infer something about the unknown source altitude of the latter. The results suggest a new method of estimating electron density profiles poleward of the aurora and provide evidence about the range of source altitudes of MFB. Section 2 describes the instrumentation and initial data analysis, section 3 describes the ray tracing analysis, and section 4 discusses the implications of the ray tracing results for the MFB generation mechanism.

2. Methodology

2.1. Instrumentation

The data for this study were collected using an array of antennas in Sondrestrom, Greenland, at 66.99°N, 50.95°W. Phase differences in the radio signals received by three antennas were used to calculate the signals' directions of arrival in three-dimensional space. The antennas used in this experiment were the reference antenna, located at the vertex of the right-angled arrangement, and two antennas each located approximately 50 m from the reference. Each antenna is a single-loop magnetic dipole antenna with area 10 m^2, with the loops of the antennas oriented parallel to one another. A preamplifier at the base of each antenna converts the induced current into a voltage, which is amplified and buffered to drive the signal down a

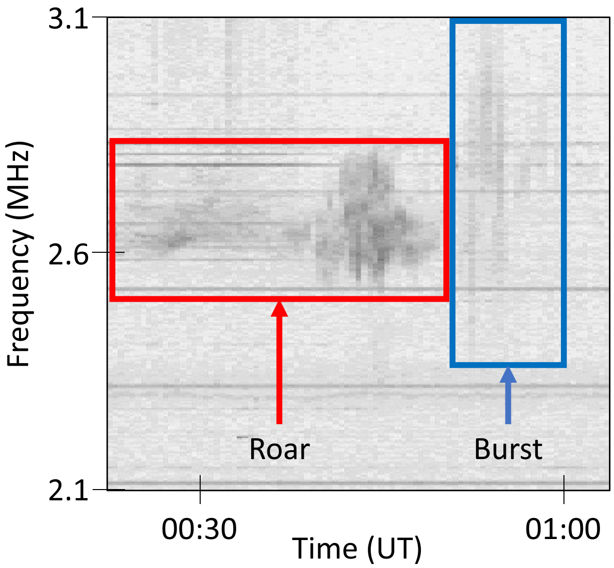

Figure 1. Power spectrogram showing a burst-roar co-occurrence event on 19 March 2013. Roar and burst are identified by the red and blue boxes, respectively. Artificially generated radio signals are visible in this figure as horizontal lines. Pixels from these signals were excluded from the analysis through careful drawing of smaller boxes of pixels within the large boxes shown here.

coaxial cable to the receiver. Hughes et al. (2000) provide further details about another instrument at Sondrestrom with electronics similar to those of the instrument used in this study.

The frequency range of the instrument, 0.1 to 3.1 MHz, is divided into four 750-kHz bands. The lowest band uses antennas on a 400-m baseline, and the upper three bands use antennas on a 50-m baseline as described above. Only the upper three bands were used in this study. A fast Fourier transform (FFT) algorithm was applied to the time series data, producing spectral data in the form of frequency versus time, which were plotted on spectrograms. Next, cross-spectral analysis was performed, producing files containing the coherence, azimuth, elevation, and power for each frequency at each time. One set of files was produced with a relatively short FFT (1,024 points), with approximately 5-s time resolution and 6.5-kHz frequency resolution. A second set of files was produced with a longer FFT (4,096 points), yielding an 18-s time resolution and a 1.6-kHz frequency resolution.

Azimuth and elevation were determined using the distances between the antennas and the phase differences between the signals at each antenna. Time corrections, directly measured in the field, were applied to account for the signals' travel times through the cables from the antennas to the receiver. The direction-finding method was confirmed using both commercial radio station signals and radio signals generated with a beacon in the field.

2.2. Event Selection

Available data from this instrument spanned from February 2013 to January 2017, with a total of 1,139 days of data available. Each day's spectrogram was searched visually for suitable burst-roar co-occurrence events. Suitable events were those which were sufficiently stronger than background noise levels, had burst and roar events occurring close together in time, and had roar occur before burst. The last criterion was necessary to ensure a similar propagation environment for both roar and burst signals, because burst indicates substorm onset, which creates a chaotic propagation environment for radio signals and makes directions of subsequent signals difficult to interpret.

Burst and roar were distinguished by visual examination of spectrograms. Burst has a wide range of frequencies and a short duration, whereas roar often occurs over relatively long durations but is confined to a narrow frequency range, approximately 2.65–2.85 MHz at Sondrestrom. It is possible to classify most emission events as burst or roar according to these criteria, but when an event of short duration occurs within the frequency range of roar, it may not be evident whether the event is roar or burst. These ambiguous events were discarded.

Boxes defining time and frequency ranges of interest were drawn, taking care to avoid contamination from artificially generated radio signals and from multiple or unknown kinds of auroral radio signals. Figure 1 shows one of the events selected for analysis with roar and burst identified.

Thirty-three suitable events were found, dating from between 2 February 2013 and 8 December 2016. The events were distributed evenly throughout the year, with one to five events taking place during each month from August through May, except for October, which had 10 events. As expected, no suitable events were found in June or July, as these months in the Arctic are dominated by sunlight, which creates *D* region ionization, resulting in absorption of medium-frequency (MF) and lower HF radio waves. Times of events were distributed fairly uniformly between 2000 and 0600 UT, tending to occur before magnetic midnight (just before 0300 UT at Sondrestrom). Roar frequencies were tightly confined, as expected, to a narrow frequency band between about 2.5 and 2.9 MHz, and all roar events had median frequencies between 2.7 and 2.8 MHz. Burst frequencies ranged more widely, with event medians ranging from 1.5 MHz to 3.0 MHz and individual burst frequencies as low as 1.2 MHz and as high as 3.1 MHz, the upper limit of the receiver.

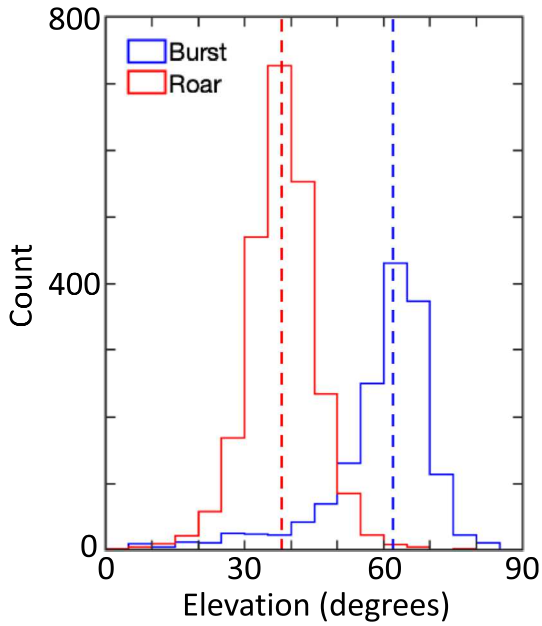

Figure 2. Elevation histograms of burst-roar co-occurrence event on 19 March 2013. The red and blue histograms display the elevation distributions of roar and burst pixels, respectively, binned by 5°. The dashed lines indicate the medians of each distribution, which are 38° and 62° for roar and burst, respectively.

Simple statistical analyses were performed on the signals' directions of arrival. Figure 2 shows a histogram of elevation angles of origin for all boxed pixels in one event, with the blue distribution representing burst, and the red distribution representing roar. In 28 of the 33 events, the median burst pixel arrived from a higher elevation angle than the median roar pixel. Figure 3 shows median azimuths and elevations for the burst and roar components of each event. The roar pixels show a bias toward the southeast, matching the findings presented in Figure 3 of Hughes et al. (2001). A potential explanation for this eastward bias is that substorm activity generally moves from east to west, and therefore burst-roar events associated with a substorm to the west of the instrument are more likely to fail the selection criteria for this study, because the ionosphere at the time of their arrival is likely to be disturbed. Bunch et al. (2009) noted a similar southeastward bias for burst events, but the burst azimuths in the present study were distributed evenly around coordinated geomagnetic (CGM) south.

3. Ray Tracing Analysis

A ray tracing algorithm was used to determine the paths taken by the roar and burst rays through the ionosphere. To obtain a density profile through which to trace the rays for each event, roar pixels were traced into the International Reference Ionosphere 2012 (IRI; Bilitza et al., 2014) profile at the receiver site for each corresponding day. The frequency condition $\boldsymbol{f = 2f_{ce}}$ required for $2f_{ce}$ roar generation was used to determine a “target height” for each roar ray, and the fraction of the pixels reaching their target heights was calculated. The electron gyrofrequency for target height determination was calculated from International Geomagnetic Reference Field (IGRF) grid data (Thébault et al., 2015). If less than 50% of the roar pixels reached their target heights, the IRI profile was shifted down by 0.1 $\log_{10}$ cm^{-3}, meaning that density values were divided by a factor of $10^{0.1}$. The roar pixels were then traced into the newly downshifted profile. This process continued iteratively until the 50% threshold was met, at which point the downshifting stopped and the final profile was obtained. Each of the 33 events required downshifting of its density profile, and downshifts by about a factor of 10 were typical.

This method was validated, and the 50% threshold was determined, through comparison of the shifted IRI profiles with actual measurements of density from incoherent scatter radar (ISR) data on the two dates in the data set for which the Sondrestrom ISR was operating in a suitable mode. On these two dates, the ISR was operated in “composite scan” mode, scanning to the south at elevations between 30.8° and 64.5°. Figure 4 shows a comparison of the shifted IRI profile with density measurements for the 13 October 2015 event. The IRI profile for this event was shifted down by a factor of approximately 12.6 (1.1 $\log_{10}$ cm^{-3}), the amount of downshifting required for at least 50% of roar pixels to reach their target heights. Figures 4a and 4c show color plots of the electron density to the south of Sondrestrom, averaged over the three-dimensional region scanned by the radar. Figures 4a and 4b show the density before the detection of burst, corresponding to substorm onset, while Figures 4c and 4d show the density after the burst. The red curves in Figures 4b and 4d show vertical cross sections of the measured densities in the scanned volume. The blue curve in Figure 4b shows the downshifted IRI density profile, which matches well with the density measurements prior to substorm onset. Figure 5 shows similar results for the 10 May 2016 event. The IRI profile for this event was shifted down by a factor of approximately 6.3 (0.8 $\log_{10}$ cm^{-3}). Good agreement between these measured density profiles and those inferred from the method described above, using the 50% criterion, suggests that this method is a significant improvement over using IRI alone to determine the density profiles.

The azimuths of roar and burst signals generally differed. For example, in the event illustrated in Figure 6, the median burst and roar azimuths differ by 34.5°. However, the methodology assumes that in the undisturbed polar cap, poleward of the aurora, the density is laminar and longitudinally uniform. These

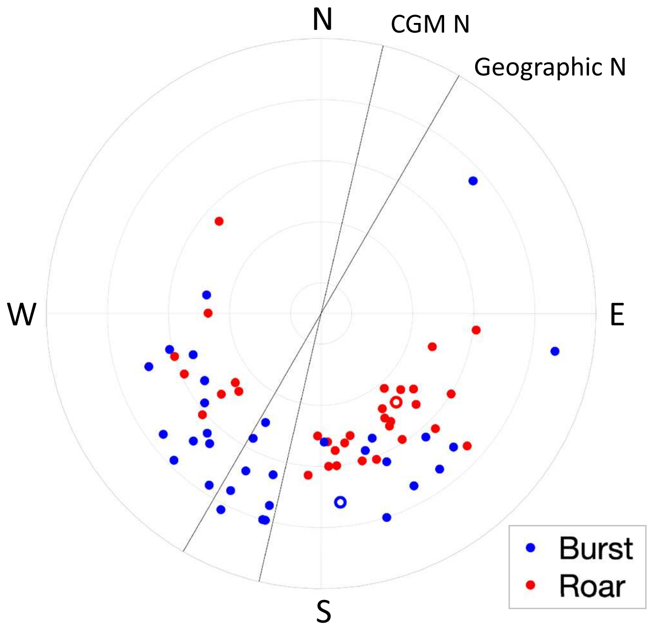

Figure 3. Polar plot of median azimuth and elevation for each burst-roar co-occurrence event. Blue and red points indicate burst and roar pixels, respectively. The open circles represent the 19 March 2013 event. The polar angle indicates the azimuth, and the distance from the center indicates the elevation, with gray circles at 10°, 30°, 50°, 70°, and 90°. Directions (N, E, S, W) are in local magnetic coordinates, with lines added to show coordinated geomagnetic (CGM) north and geographic north.

conditions make ray tracing comparable among signals with different azimuths. The same assumptions apply to the density profiles measured by the Sondrestrom ISR, shown in Figures 4 and 5.

After the density profile was set, burst pixels were ray traced into it, as shown in Figure 6. In order to know when to terminate the traced rays, it is necessary to know the approximate location of the polewardmost auroral arc, from which the observed signals may have originated. The location of this arc was set using the horizontal position at which the 90th-percentile-elevation roar ray reached its target height. The rationale for choosing the 90th-percentile ray is that most of the other roar rays likely originate from more distant sources in the main central band of auroral arcs rather than the polewardmost arc. The highest-elevation roar rays are most likely to originate in or near the polewardmost arc, but the rays with the very highest elevation angles may be disproportionately likely to be affected by error. Accordingly, accounting for random error and uncertainty in the elevation measurements, the horizontal distance at which the 90th-percentile roar ray encounters its source is taken to be a good measure of the location of the polewardmost arc.

Figure 6 shows ray traces of burst signals (blue) and roar signals (red) for a selected event occurring on 8 December 2016. The roar source height, where $f = 2f_{ce}$, is different for each ray, but the white horizontal dashed line shows its average value for this event: 250 km, somewhat lower than the typical roar source height of 275 km (Hughes & LaBelle, 1998). The background color scale shows the density profile used for the ray tracing, which was determined by the criterion that 50% of the roar rays reach their source altitudes. The white vertical dashed line shows the downrange distance at which the 90th-percentile roar ray reaches its source altitude. This distance (125 km) is taken to be the distance to the polewardmost arc, and the distribution of altitudes of the burst rays at this distance can then be obtained. If the burst originates at the polewardmost arc, as suggested by some previous

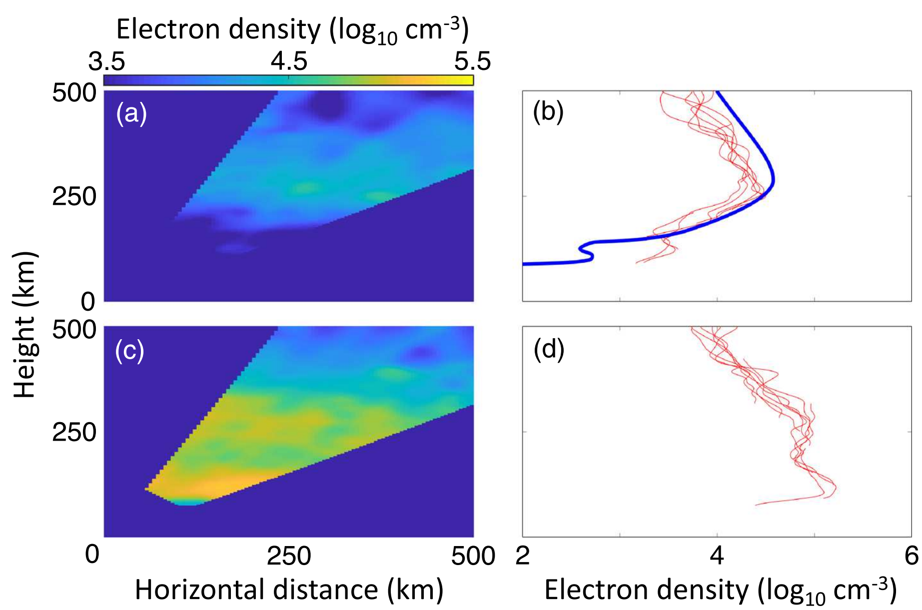

Figure 4. Density data from burst-roar event on 13 October 2015. Left panels show density as measured by radar (a) before and (c) after the burst event. The dark blue region outside the wedge of observations represents areas where no density measurements were made. Panels (b) and (d) show vertical cross sections through the measured density (red), spaced horizontally at 50-km intervals, in comparison with the shifted IRI profile (blue).

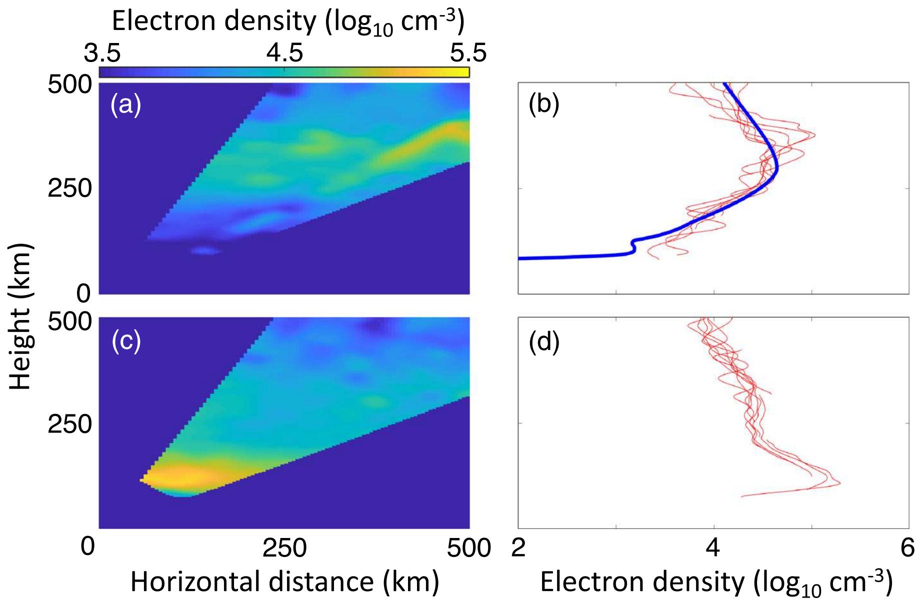

Figure 5. Same as Figure 4 for the event on 10 May 2016.

experiments (Bunch et al., 2009), then this measurement would give the distribution of burst source heights. Ray tracing indicates that some burst rays originate from the ground at a downrange distance less than that of the estimated location of the polewardmost arc. In the example shown in Figure 6, the burst source heights, that is, the heights where the burst rays (shown in blue) intersect the vertical dashed white line, range from 0 to 490 km, with a median of 184 km. The histogram of burst source heights for this event is shown in the last panel of Figure 7.

Figure 7 shows histograms of burst source heights for each of the 33 events, binned by 50 km, with the events represented in chronological order along each row and in successive rows, so that the first event is represented in the first panel of the first row, the second event is in the second panel in the first row, the twelfth event is in the first panel of the second row, and so on. The bottom right panel shows the last of the events in this study, which is the 8 December 2016 event plotted in Figure 6. All source heights between 0 and 500 km are represented in the histograms, though most events have few or no burst sources above 300 km. Among all 33 histograms, the average of the median burst source height of each histogram is 172 km with an average standard deviation of 87 km. The mode of the distribution of median burst source heights, binned by 50 km, is the 200–250 km bin.

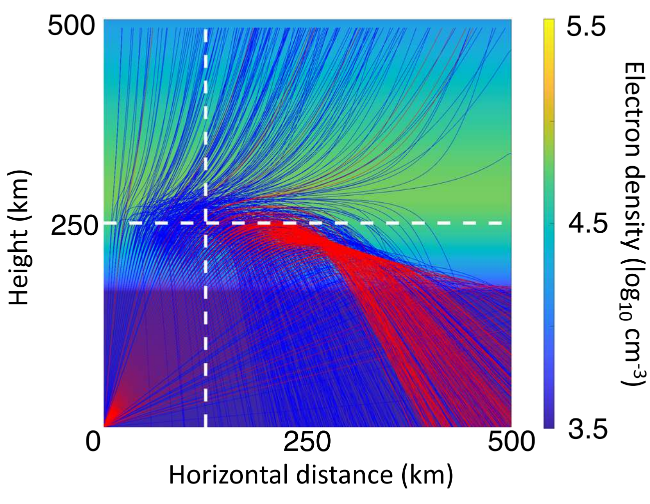

Figure 6. Ray traces of 8 December 2016 burst-roar event. Burst and roar ray paths as determined from ray tracing are shown in blue and red, respectively. The background color scale indicates the electron density given by the downshifted IRI profile. The white horizontal dashed line shows the average roar source height. The white vertical dashed line indicates the horizontal distance at which the 90th-percentile roar ray by elevation angle reaches its target height.

As Figure 7 shows, most events have a peak in the burst source height distribution around 200 km, suggesting that in most of these events, the predominant source of burst rays occurs at this altitude. Of the 33 histograms of burst source heights, 6 have maximum bin count in the bin that ranges from 250 to 300 km, 15 have maximum bin count from 200 to 250 km, 3 have maximum bin count from 150 to 200 km, 1 has maximum bin count in the bin from 100 to 150 km, and the remaining 8 have maximum bin count in the bin from 0 to 50 km (the ground-level bin). Among the 25 events whose burst source height distributions peak above ground level, the median burst source heights range from 139 to 296 km, with a mean value of 208 km. This mean value provides an estimate of the burst source height of a typical burst-roar co-occurrence event. Among these same 25 events, the mean of the standard deviations of each distribution of burst

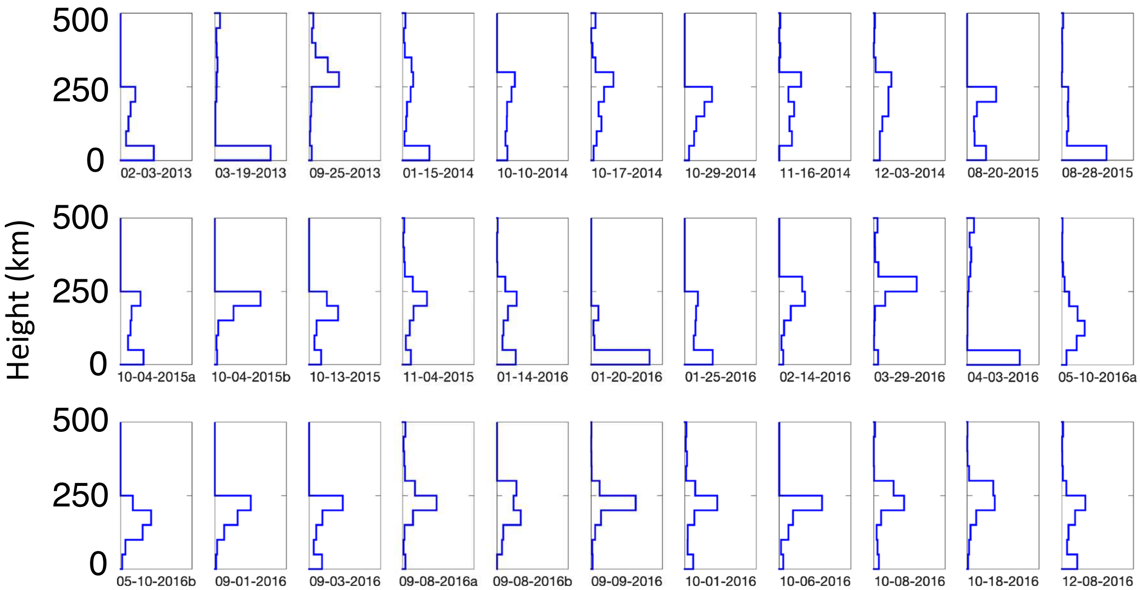

Figure 7. MFB source height histograms for each event, binned by 50 km from 0 to 500 km. The horizontal axis of each histogram is normalized by the total number of MFB pixels in the corresponding event. Each histogram is labeled with the date of the event, and an "a" or "b" following the date to identify events that occur on dates with multiple events.

source heights is 78 km. Since these events provide an ensemble of possibilities for a typical burst-roar co-occurrence event, this average standard deviation provides an estimate of the uncertainty in the typical burst source height.

Many of the histograms of burst source height also show peaks at ground level. Eight of the burst source height histograms have maximum bin counts at ground level, and several other histograms show secondary peaks in the ground-level bin. These peaks near ground level are presumed to occur in cases where the distance to the polewardmost auroral arc has been overestimated. Most of the eight events with maximum bin counts at ground level show secondary peaks around 250 km, likely corresponding to burst emissions from sources further downrange than the estimated location of the polewardmost arc.

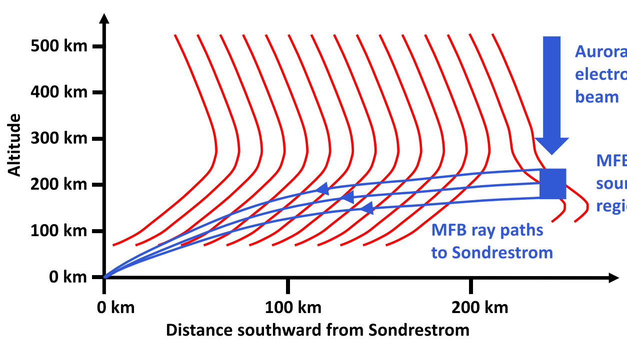

Figure 8. Illustration of the proposed conditions for observation of MFB at Sondrestrom. The horizontal axis represents distance southward from Sondrestrom, and the vertical axis represents altitude. Burst rays detected at Sondrestrom originate at the polewardmost auroral arc, indicated by a downward arrow representing the auroral electron beam. At this location, the electron density profile (shown in red) peaks in the *E* region, whereas it peaks in the *F* region at locations poleward of the arc. Burst is generated at a range of altitudes centered on 200 km and refracts through the relatively laminar density profiles poleward of the arc to reach Sondrestrom.

4. Discussion

In 25 of the 33 events plotted in Figure 7, most burst pixels originate from altitudes around 200 km. To explain burst generation at this altitude, we put forth the model shown in Figure 8. In this figure, the vertical axis represents altitude, and the horizontal axis represents distance southward from Sondrestrom. In this model, as Figure 8 shows, the density profile is laminar in the polar cap, north of the polewardmost expanding substorm auroral arc, with density peaking in the *F* region, consistent with the ISR profiles shown in Figures 4a, 4b, 5a, and 5b. By contrast, the density profile underneath the polewardmost expanding substorm arc peaks in the *E* region, due to the intense auroral precipitation. Evidence for this distorted electron density profile underneath the advancing arc is provided by Figures 4c, 4d, 5c, and 5d, which show the enhanced density in the *E* region observed when the substorm arc has come overhead of Sondrestrom after MFB occurrence. This same result was noted by Broughton et al. (2012), shown in Figure 4 of that paper. The laminar density profile between the antenna array at Sondrestrom and the polewardmost arc allows the emitted radiation to access and be detected by the antenna array. In contrast to roar, which originates at a specific source height where its frequency-matching condition is met, burst source heights can be more widely distributed. Figure 8 illustrates MFB coming from sources at 140–300 km, corresponding to the range of median burst source heights of the 25 histograms with maximum bin counts above ground level.

Figures 4c, 4d, 5c, and 5d, as well as Figure 4 of Broughton et al. (2012), which show the density profiles following MFB occurrence, illustrate how the density profile is distorted under the expanding substorm arc, with peak density at about 100–150 km, in the *E* region rather than in the *F* region. The MFB sources are therefore in a region of downward pointing density gradient, even though they are at relatively low altitudes of approximately 200 km. Accordingly, MFB generation at this altitude is qualitatively consistent with the model proposed by LaBelle (2011), which explains the detailed frequency structure of MFB as resulting from dispersion of downward propagating Langmuir waves generated on a downward pointing density gradient. However, further modeling efforts are needed to confirm whether this model is quantitatively consistent with the source altitudes found in Figure 7, since the applications of the model shown in Figure 3 of LaBelle (2011) are at somewhat higher altitudes. Propagation to ground level should be possible as long as the MFB frequency exceeds the maximum *L* cutoff frequency below the source, as explained by LaBelle (2011) and Broughton et al. (2015).

In the events with burst source height distributions that have strong peaks at ground level, we propose that the range to the auroral arc has been overestimated by our choice of the 90th-percentile roar ray. Alternatively, it is possible that the range to the auroral arc has been estimated correctly, but some of the burst rays emanating from the source reflected off the ground before reaching Sondrestrom. The burst source height distributions in some of these cases show a secondary peak in the distribution at a reasonable height, perhaps corresponding to the burst rays that have not reflected off the ground. The possibility of a local density anomaly provides another potential explanation for the peaks near ground level.

As a byproduct of this study, we propose a new method of estimating density profiles in the polar cap, by using roar rays to modify the IRI density profile via downshifting, as we have done, or upshifting, if necessary. This method need not apply only to burst-roar co-occurrence events: since roar occurs often throughout the night, this technique could be used frequently. In future work, this method could be better validated with more events. Furthermore, though we modify the IRI profiles only by scaling the density by a constant factor, modifying it in other ways might further optimize density estimation. Separately, as an additional area for potential future refinements, if further studies better constrain the altitudes of origin of roar and burst, then source altitude could itself be used as a diagnostic for distinguishing roar and burst in some of the ambiguous cases we had to discard.

In summary, we establish that among the 25 events with peaks above ground level, median MFB source heights range from 139 to 296 km with a median of 208 km. These sources appear to be on the topside of the density profile, with the profile peaking in the *E* region, qualitatively consistent with the mechanism of generation of MFB from mode conversion of Langmuir waves excited at a range of altitudes, hence a range of plasma frequencies, on the topside ionosphere (Broughton et al., 2015; LaBelle, 2011). Our findings present the possibility of a new method of estimating polar cap density based on these measurements.

Conflict of Interest

The authors declare no conflicts of interest.

Data Availability Statement

Data used to determine directions of arrival are available through LaBelle (2020).

Acknowledgments
We thank Terrence Kovacs and David McGaw for technical assistance with this project. Sources of funding for this project include National Science Foundation Grant AGS-1915058 to Dartmouth College, the NASA New Hampshire Space Grant, the James O. Freedman Presidential Scholars Program, and the Dartmouth College Wilder Fellowship.

References

Akbari, H., Semeter, J. L., Nicolls, M. J., Broughton, M., & LaBelle, J. (2013). Localization of auroral Langmuir turbulence in thin layers. *Journal of Geophysical Research: Space Physics*, *118*, 3576–3583. https://doi.org/10.1002/jgra.50314

Benson, R. F., & Desch, M. D. (1991). Wideband noise observed at ground level in the auroral region. *Radio Science*, *26*(4), 943–948. https://doi.org/10.1029/91RS00450

Benson, R. F., & Wong, H. K. (1987). Low-altitude ISIS 1 observations of auroral radio emissions and their significance to the cyclotron maser instability. *Journal of Geophysical Research*, *92*(A2), 1218–1230. https://doi.org/10.1029/JA092iA02p01218

Bilitza, D., Altadill, D., Zhang, Y., Mertens, C., Truhlik, V., Richards, P., et al. (2014). The International Reference Ionosphere 2012—A model of international collaboration. *Journal of Space Weather and Space Climate*, *4*(A07), 1–12. https://doi.org/10.1051/swsc/2014004

Broughton, M. C., LaBelle, J., Kim, E.-H., Yoon, P. H., Johnson, J. R., & Cairns, I. H. (2016). On the propagation and mode conversion of auroral medium frequency bursts. *Journal of Geophysical Research: Space Physics*, *121*, 1706–1721. https://doi.org/10.1002/2015JA021851

Broughton, M. C., LaBelle, J., & Parrot, M. (2015). DEMETER observations of bursty MF emissions and their relation to ground-level auroral MF burst. *Journal of Geophysical Research: Space Physics*, *119*, 144–155. https://doi.org/10.1002/2014JA020410

Broughton, M. C., LaBelle, J., Roberg-Clark, G. T., McCready, M., & Bunch, N. L. (2012). Experimental tests of a topside generation mechanism for auroral medium frequency radio emissions. *Journal of Geophysical Research*, *117*, A12309. https://doi.org/10.1029/2012JA018034

Budden, K. G. (1985). *The propagation of radio waves: The theory of radio waves of low power in the ionosphere and magnetosphere*. Cambridge, United Kingdom: Cambridge University Press. https://doi.org/10.1017/CBO9780511564321

Bunch, N. L., & LaBelle, J. (2009). Fully resolved observations of auroral medium frequency burst radio emissions. *Geophysical Research Letters*, *36*, L15104. https://doi.org/10.1029/2009GL038513

Bunch, N. L., LaBelle, J., Weatherwax, A. T., Hughes, J. M., & Lumerzheim, D. (2009). Experimental tests of the generation mechanism of auroral medium frequency burst radio emissions. *Journal of Geophysical Research*, *114*, A09302. https://doi.org/10.1029/2008JA013993

Hughes, J. M., & LaBelle, J. (1998). The latitude dependence of auroral roar. *Journal of Geophysical Research*, *103*(A7), 14,911–14,915. https://doi.org/10.1029/98JA01038

Hughes, J. M., & LaBelle, J. (2001). Plasma conditions in auroral roar source regions inferred from radio and radar observations. *Journal of Geophysical Research*, *106*(A10), 21,157–21,164. https://doi.org/10.1029/2001JA000010

Hughes, J. M., LaBelle, J., & Trimpi, M. L. (2000). A medium-frequency interferometer for studying auroral radio emissions. *Review of Scientific Instruments*, *71*(8), 3200–3206. https://doi.org/10.1063/1.1305518

Hughes, J. M., LaBelle, J., & Watermann, M. (2001). Statistical and case studies of $2f_{ce}$ auroral roar observed with a medium frequency interferometer. *Journal of Geophysical Research*, *106*(A10), 21,147–21,155. https://doi.org/10.1029/2001JA000009

James, H. G., Hagg, E. L., & Strange, L. P. (1974). Narrowband radio noise in the topside ionosphere. AGARD Conference Proceedings, AGARD-CP-138, 24.

Kaufmann, R. (1980). Electrostatic wave growth: Secondary peaks in a measured auroral electron distribution function. *Journal of Geophysical Research*, *85*(A4), 1713–1721. https://doi.org/10.1029/JA085iA04p01713

Kellogg, P. J., & Monson, S. J. (1979). Radio emissions from the aurora. *Geophysical Research Letters*, *6*(4), 297–300. https://doi.org/10.1029/GL006i004p00297

LaBelle, J. (2011). An explanation for the fine structure of MF burst emissions. *Geophysical Research Letters*, *38*, L03105. https://doi.org/10.1029/2010GL046218

LaBelle, J. (2012). First observations of $5f_{ce}$ auroral roars. *Geophysical Research Letters*, *39*, L19106. https://doi.org/10.1029/2012GL053551

LaBelle, J. (2020). *Replication data for: Estimating polar cap density and medium frequency burst source heights using $2f_{ce}$ roar radio emissions, Version 1*. Cambridge, MA: Harvard Dataverse. https://doi.org/10.7910/DVN/CQITZB

LaBelle, J., & Treumann, R. A. (2002). Auroral radio emissions, 1. Hisses, roars, and bursts. *Space Science Reviews*, *101*(3/4), 295–440. https://doi.org/10.1023/A:1020850022070

Samara, M., LaBelle, J., Kletzing, C. A., & Bounds, S. R. (2004). Rocket observations of structured upper hybrid waves at $f_{uh} = 2f_{ce}$. *Geophysical Research Letters*, *31*, L22804. https://doi.org/10.1029/2004GL021043

Sato, Y., Ono, T., Sato, N., & Fujii, R. (2010). MF/HF auroral radio emissions emanating from the topside ionosphere. *Geophysical Research Letters*, *37*, L14102. https://doi.org/10.1029/2010GL043731

Sato, Y., Ono, T., Sato, N., & Ogawa, Y. (2012). First observations of $4f_{ce}$ auroral roar emissions. *Geophysical Research Letters*, *39*, L07101. https://doi.org/10.1029/2012GL051205

Shepherd, S. G., LaBelle, J., & Trimpi, M. L. (1997). The polarization of auroral radio emissions. *Geophysical Research Letters*, *24*(24), 3161. https://doi.org/10.1029/97GL03160

Thébault, E., Finlay, C. C., Beggan, C. D., Alken, P., Aubert, J., Barrois, O., et al. (2015). International Geomagnetic Reference Field: The 12th generation. *Earth, Planets and Space*, *67*(1), 79. https://doi.org/10.1186/s40623-015-0228-9

Weatherwax, A. T., LaBelle, J., & Trimpi, M. L. (1994). A new type of auroral radio emission at 1.4–3.7 MHz observed from the ground. *Geophysical Research Letters*, *21*. https://doi.org/10.1029/94GL02512

Weatherwax, A. T., LaBelle, J., Trimpi, M. L., & Brittain, R. (1993). Ground based observations of radio emissions near $2f_{ce}$ and $3f_{ce}$ in the auroral zone. *Geophysical Research Letters*, *20*(14), 1447–1450. https://doi.org/10.1029/GL020i014p01447

Yoon, P. H., Weatherwax, A. T., & Rosenberg, T. J. (1998). On the generation of auroral radio emissions at harmonics of the lower ionospheric electron cyclotron frequency: X, O and Z mode maser calculations. *Journal of Geophysical Research*, *103*(A3), 4071–4078. https://doi.org/10.1029/97JA03526

Yoon, P. H., Weatherwax, A. T., Rosenberg, T. J., & LaBelle, J. (1996). Lower ionospheric cyclotron maser theory: A possible source of $2f_{ce}$ and $3f_{ce}$ auroral radio emissions. *Journal of Geophysical Research*, *101*(A12), 27,015–27,025. https://doi.org/10.1029/96JA02664

Yoon, P. H., Weatherwax, A. T., Rosenberg, T. J., LaBelle, J., & Shepherd, S. G. (1998). Propagation of medium frequency (1–4 MHz) auroral radio waves to the ground via the Z-mode radio window. *Journal of Geophysical Research*, *103*(A12), 29,267–29,275. https://doi.org/10.1029/1998JA900032